Research Square

Preprints are preliminary reports that have not undergone peer review.
They should not be considered conclusive, used to inform clinical practice,
or referenced by the media as validated information.

Satellites detect methane outburst driven by magma-sediment interactions

Edna Dualeh

edna.dualeh@bristol.ac.uk

University of Bristol https://orcid.org/0000-0003-2933-3039

Juliet Biggs

University of Bristol https://orcid.org/0000-0002-4855-039X

Shubham Sharma

SRON Netherlands Institute for Space Research

John Stix

Department of Earth & Planetary Sciences, McGill University

William Hutchison

University of St Andrews https://orcid.org/0000-0002-5456-3277

Giuseppe Etiope

Istituto Nazionale di Geofisica e Vulcanologia, Rome, Italy https://orcid.org/0000-0001-8614-4221

Dylan Jervis

GHGSat, Inc.

Lin Way

University of Bristol https://orcid.org/0000-0002-3781-2227

Matthieu Dogniaux

SRON Space Research Organisation Netherlands https://orcid.org/0009-0009-8870-8073

Joannes Maasakkers

SRON Netherlands Institute for Space Research https://orcid.org/0000-0001-8118-0311

Simone Aveni

Università degli Studi di Torino

Daniel H. Cusworth

Carbon Mapper https://orcid.org/0000-0003-0158-977X

Ben Ireland

University of Bristol

Raphaël Grandin

IPGP https://orcid.org/0000-0002-1837-011X

Marianne Girard

GHGSat Inc.

Antoine Ramier

GHGSat Inc.
Weiyu Zheng
University of Bristol
Timothy Davis
University of Bristol
Katherine Howell
University of Michigan
Diego Coppola
Università degli Studi di Torino https://orcid.org/0000-0001-7181-4122
Arthur Hauck
IPGP https://orcid.org/0009-0001-7701-0114
Richard Pancost
University of Bristol
Meredith Nettles
Columbia University https://orcid.org/0000-0003-4613-4162
Elias Lewi
Addis Ababa University

Physical Sciences - Article

Keywords: Satellite-based remote-sensing, methane emissions, magma sediment interac

Posted Date: March 12th, 2026

DOI: https://doi.org/10.21203/rs.3.rs-8435396/v1

License: This work is licensed under a Creative Commons Attribution 4.0 International License.
Read Full License

Additional Declarations: There is **NO** Competing Interest.

Version of Record: A version of this preprint was published at Nature Geoscience on November 19th, 2026. See the published version at https://doi.org/10.1038/s41561-026-02137-4.

Satellites detect methane outburst driven by magma-sediment interactions

Dualeh, EW[1]*, Biggs, J[1], Sharma, S[2], Stix, J[3], Hutchison, W[4], Etiope, G[5,6], Jervis, D[7], Way, L[1], Dogniaux, M[2], Maasakkers, J.D[2], Aveni, S[8,9], Cusworth, D[10], Ireland, B[1], Grandin, R[11], Girard, M[7], Ramier, A[7], Zheng, W[1], Davis, T[1], Howell K[10,12], Coppola, D[8], Hauck, A[11], Pancost, RD[1], Nettles, M[13], Lewi, E[14].

[1*]COMET, School of Earth Sciences, University of Bristol, Bristol, UK; [2]SRON Space Research Organisation Netherlands, Leiden, Netherlands; [3]Department of Earth & Planetary Sciences, McGill University, Canada; [4]School of Earth and Environmental Sciences, University of St Andrews, St Andrews, UK; [5]Istituto Nazionale di Geofisica e Vulcanologia (INGV), Rome, Italy; [6]Faculty of Environmental Science and Engineering, Babes-Bolyai University, Cluj-Napoca, Romania; [7]GHGSat Inc., Montreal, Quebec, Canada; [8]Department of Earth Sciences, University of Turin, Turin, Italy; [9]Department of Civil, Constructional and Environmental Engineering (DICEA), Sapienza University of Rome, Rome, Italy; [10]Carbon Mapper, Pasadena, United States; [11]Institut de Physique du Globe de Paris (IPGP), Université Paris Cité, CNRS, Paris, France; [12]College of Engineering, University of Michigan, Michigan, ISA; [13]Lamont-Doherty Earth Observatory (LDEO), Columbia University, Palisades, USA; [14]Institute of Geophysics, Space Science and Astronomy, Addis Ababa University, Addis Ababa, Ethiopia

*Corresponding author(s). E-mail(s): edna.dualeh@bristol.ac.uk

Abstract

Magmatic intrusions into sedimentary rocks can release carbon-based greenhouse gases, dominantly methane, and have been linked to rapid changes in past climate. However, we lack appropriate modern analogues, as most volcanic systems emit very little methane. Here, we report the first confirmed satellite detection of methane emissions from a volcanic system, likely resulting from interactions between magma and sedimentary rocks. In early 2025, Fentale Volcano (Ethiopia) released >38.2 ± 3.9 kilo tonnes of methane, of which 90% was emitted within 31 days. The peak emission rate of 157 ± 41 tonnes per hour is comparable to major industrial blowouts and ~4 orders of magnitude higher than the methane emission rates of other volcanic systems. The emissions followed the intrusion of ~1 km^3 of magma into a dyke which did not erupt. Subsequent emissions of methane and carbon dioxide coincided with localised ground subsidence and thermal anomalies within Fentale's caldera. We infer that the intrusion disrupted an impermeable cap beneath which methane, derived from hydrocarbon-rich sediments, was trapped. This single outburst is small compared to annual emissions from natural and anthropogenic sources, but demonstrates that some volcanoes can release methane episodically, providing insight into the mechanism of greenhouse gas release in magmatic-sedimentary systems

Keywords: Satellite-based remote-sensing; methane emissions; magma sediment interactions

1 Main

Methane is a major greenhouse gas with warming potential roughly 81 times that of carbon dioxide (CO_2) over 20 years[1]. It is considered a key driver of rapid perturbations in both past and present climate[2]. Direct anthropogenic sources account for >50% of the current global methane budget[3]. Accurate climate forecasting requires robust quantification of both natural and anthropogenic sources but uncertainties on natural emissions remain large[3].

Measured methane emissions rates at volcanic systems are typically low (Fig. 1C) and account for <1% of the total atmospheric methane budget[4–6]. Methane is only present in trace amounts in magmatic gases[7] but in significant quantities in hydrocarbon-rich sedimentary basins, which represent the major natural source of fossil methane[6]. Therefore, methane could be released by systems where magma interacts with sedimentary rocks[4,8]. Exceptional magmatic events, such as Large Igneous Provinces (LIPs), have been linked to rapid climate change throughout Earth's history[9]. Models suggest that thermal maturation of organic matter within sedimentary rocks could release carbon-based greenhouse gases on sufficiently short timescales to drive rapid global warming[2,10]. However, the only modern analogues for the release of methane by magmatic-sedimentary systems are in geothermal settings rather than volcanic systems[8,11] and are not included in compilations of the natural sources of methane[3,4].

Satellite observations have greatly improved global monitoring of volcanic gas emissions, including from passively degassing systems (Fig. 1D)[12]. However, detections remain largely limited to sulphur dioxide owing to its strong spectral features and high signal-to-noise ratio; other volcanic gases remain more difficult to detect[13]. The ever-growing number of satellite instruments developed for detecting, monitoring and locating anthropogenic greenhouse gas emissions[14] have improved our ability to monitor natural sources. Yet, to date there have been no satellite-based detections of methane from a volcanic system.

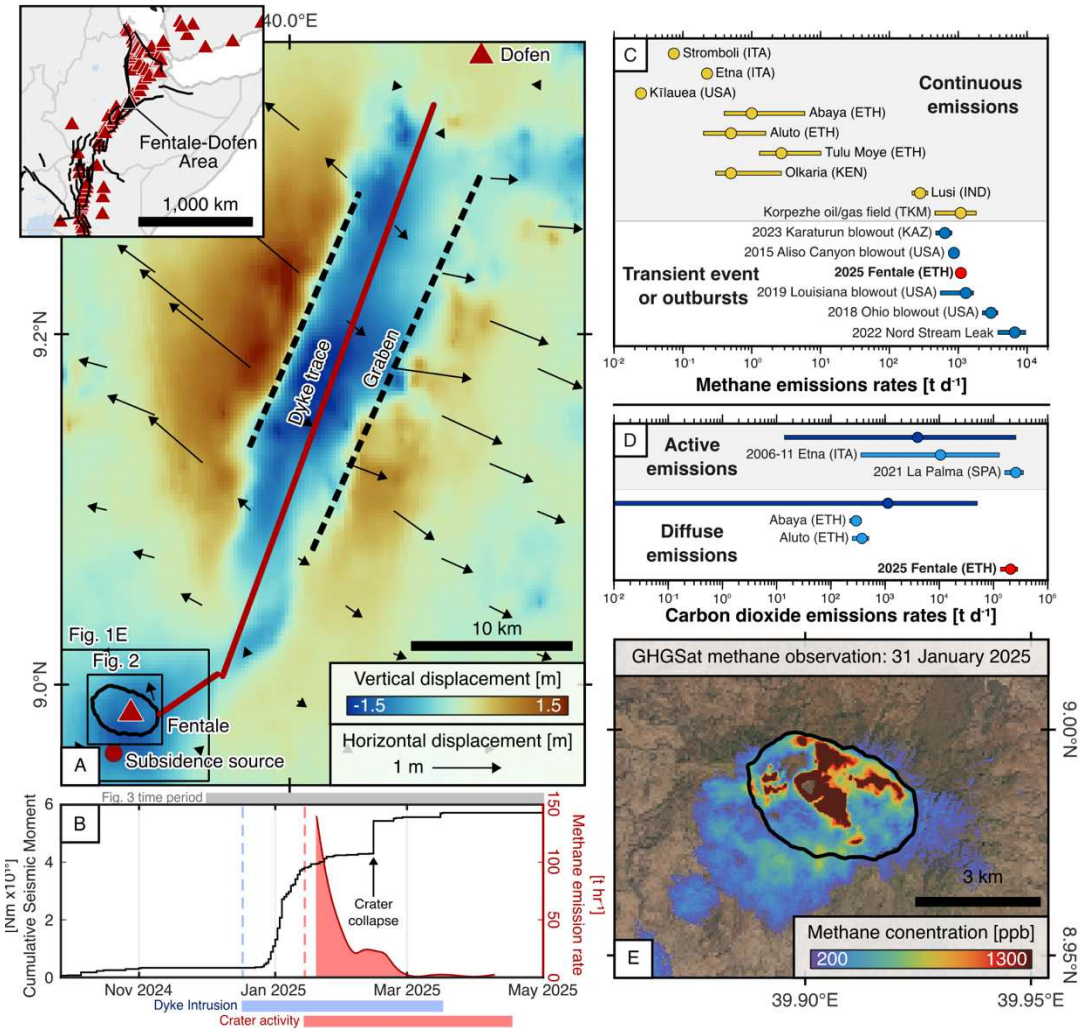

Figure 1. Overview of the 2025 Fentale volcano-seismic crisis. *(A) 3D displacement map from 16 December to 31 January showing dyke emplacement between Fentale and Dofen and subsidence under Fentale. 3D displacements are constructed from Sentinel-1 and COSMO-SkyMed (CSK) InSAR line-of-sight displacement and range offset. Insert shows the Fentale-Dofen area within the East African Rift. (B) Timeline of key activity during the 2024-2025 Fentale-Dofen unrest showing cumulative seismic moment (black line; data source: GEOFON) for the area shown in (A) and average methane emissions (red) from Fentale. (C) Compilation of methane emission rates for various systems (volcanic, natural, anthropogenic) globally split by continuous and transient event. (D) Comparison of volcanic carbon dioxide emissions for active emissions (from active volcanoes as plume or vent emissions) and diffuse emissions (from active and dormant volcanic areas). Compilations shown in dark blue and individual systems in light blue (Fig. S19). Emissions from Fentale for this period are shown in red. (E) Spatial distribution of a methane plume observed by the high resolution GHGSat satellite on 31 January 2025. The GHGSat observation shows methane enhancement above background levels.*

Here, we present the first satellite-based observation of methane emissions from a volcanic system. We use satellite observations to investigate the source, timing, and mechanism of gas release and conclude that magmatic-sediment systems, such as rifts and sedimentary-hosted geothermal systems, can be important natural sources of methane[4,8]. We propose that the Fentale outburst represents a small-scale, modern analogue of processes associated with LIPs and hyperthermal events[15,16]. This case study shows that some volcanoes can be significant methane emitters, revealing new insights into the mechanisms by which magmatic intrusions release carbon-based greenhouse gases.

2 Evolution of activity at Fentale

A magmatic intrusion initiated near Fentale Volcano on 17 December 2024, propagated ~50 km north by 29 December 2024 and continued opening until mid-March 2025 (Fig. 1A-B)[17,18]. The magma (~1 km^3) remained trapped within the subsurface and did not produce any lava flows. Methane emissions of >38.2 ± 3.9 kt were detected between 19 January and 9 April 2025, with 90% (33.8 ± 3.5 kt) released in the first month alone (Fig. 1B). Here, we focus on observations of activity within the caldera of Fentale from 14 January 2025 onwards using satellite-based thermal (VIIRS), optical (Sentinel-2 and PlanetScope) and Synthetic Aperture Radar (SAR)(COSMO-SkyMed, (CSK) and CSK Second Generation, (CSG)) imagery and measurements of trace gases (TROPOMI, GHGSat and Tanager-1)(Fig. 2-3).

The first sign of activity within the Fentale caldera was a thermal anomaly detected at 22:48 UTC on 14 January 2025 (Fig. 2J,3D). Approximately 9 hours later, we observe a cloud confined to a depression in the caldera (07:28 UTC, 15 January 2025, Text S3, Fig. S11) and spatially correlated with the thermal anomaly (Fig. 2F). The cloud's white colour and opacity suggest that it is dominated by condensed water droplets, which is supported by SAR backscatter observations of increased surface moisture (Fig. S6). Its low-lying nature indicates that it contained significant quantities of CO_2. Over the following days, the thermal anomaly intensified and both it and the low-lying plume expanded (Fig. 2J-K,3C-D).

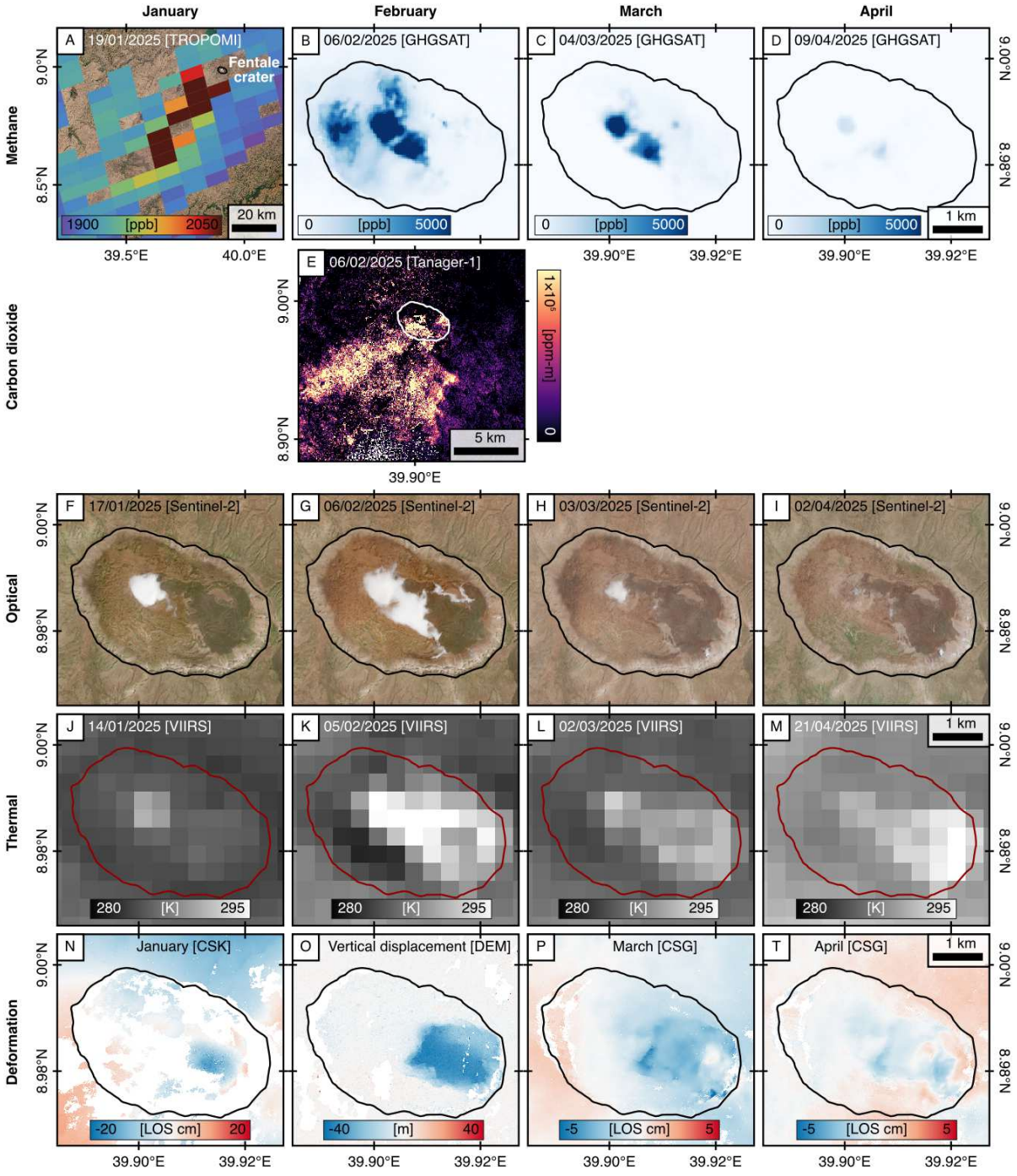

Figure 2. Spatial evolution of remote sensing observations. *(A-D) methane distribution from TROPOMI and GHGSat; (E) carbon dioxide plume from Tanager-1; (F-I) Sentinel-2 optical imagery showing a low-lying white plume; (J-M) thermal anomaly from VIIRS. (N) COSMO-SkyMed (CSK) ascending line-of-sight (LOS) displacement between 7-24 January, (O) Vertical displacement estimated from difference between the DEMs (9 January and 24 April) after correcting for the horizontal displacement and (P-T) CSK Second Generation (CSG) descending LOS displacement between 3-27 March and 4-28 April respectively.*

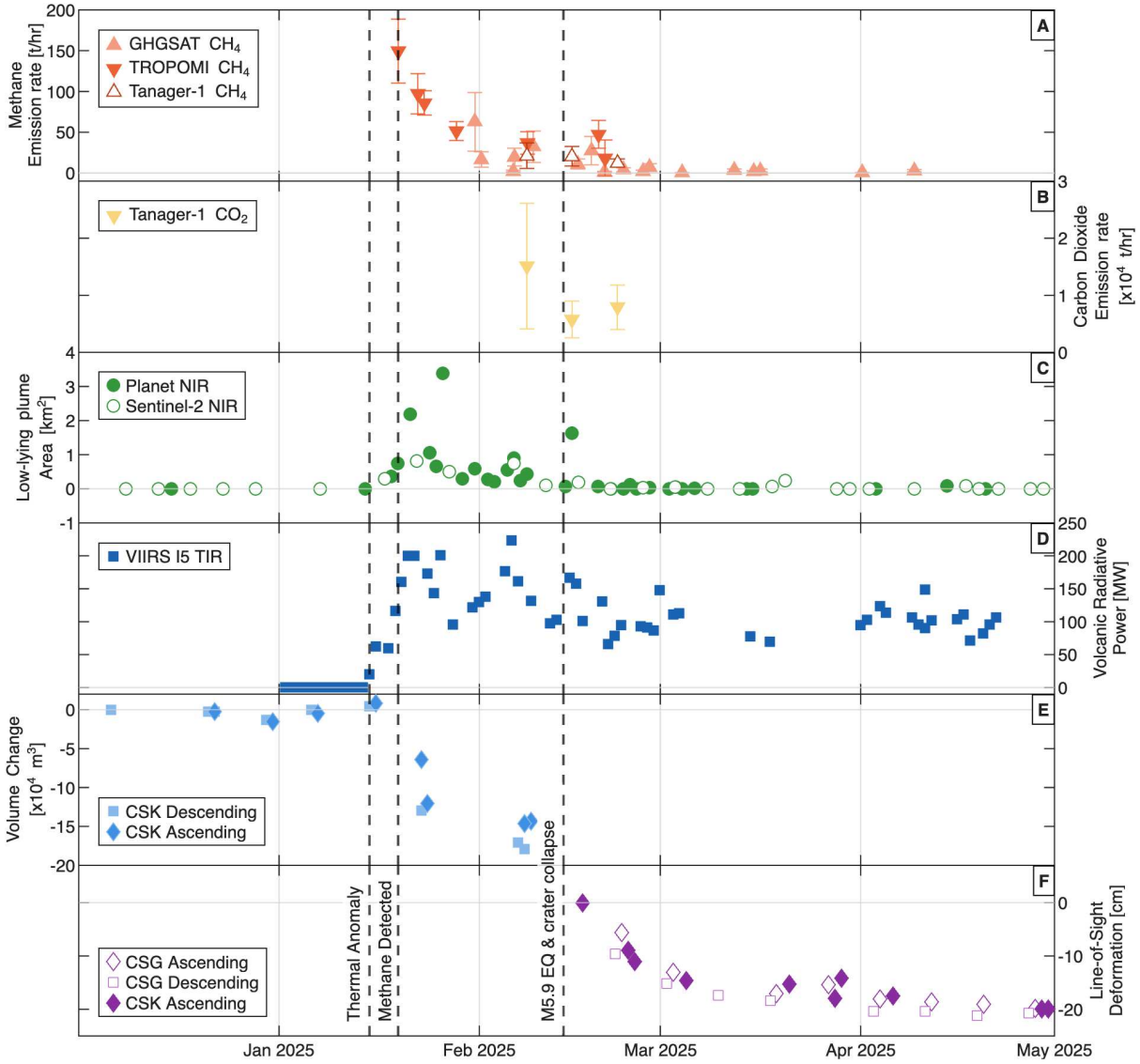

Figure 3. Temporal evolution of remote sensing observations. *(A) methane emission rate estimates from TROPOMI, GHGSat and Tanager-1; (B) carbon dioxide flux estimates from Tanager-1; (C) area of the low-lying plume within Fentale Caldera observed with Sentinel-2 and PlanetScope; (D) radiative power emission from VIIRS; (E) modelled volume change associated with localised deformation and (F) line-of-sight displacement from COSMO-SkyMed. Deformation was analysed separately (E-F) as the large collapse that occurred on 14 February 2025 changed the mechanisms associated with deformation. Dashed lines represent key activity events.*

Methane was first detected on 19 January 2025, when the TROPOMI instrument aboard European Space Agency's Sentinel-5P satellite (5.5×7 km^2 spatial resolution) detected a strong methane plume to the southwest of Fentale with an emission rate of 157 ± 41 t hr^{-1} (Fig. 3A).

Back-trajectory analysis on the initial TROPOMI plume, with planetary boundary layer averaged ERA5[19], NCEP[20] and GEOS-FP[21] wind fields, reveals that emissions began at Fentale at least 4-6 hours before the TROPOMI overpass at 10:26 UTC on 19 January (Text S1). TROPOMI images between 14 and 18 January did not show detectable quantities of methane enhancement downwind of Fentale. However, we assume that small, caldera-confined emissions may have begun on or after 14 January coincident with the first thermal anomalies. The first tasked high-resolution (25 × 25 m^2) observation from GHGSat on 31 January confirmed that methane emissions (62.8 ± 36.0 t hr^{-1}) originated from Fentale (Fig. 1E).

The first overpass of a CO_2-sensitive instrument on 5 February by GHGSat, detected CO_2 confined to depressions in Fentale. Multiple CO_2 plumes were observed throughout February by Tanager-1 and GHGSat (Fig. 2E, 3B, S3-4) with a maximum emission rate of 15,100 ± 11,000 t hr^{-1} (Table S5). In total >2.9 ± 1.0 $MtCO_2$ were emitted from Fentale over 14 days. While no casualties were reported, our estimates are significantly larger than previous volcanic CO_2 outbursts (0.047-1.2 $MtCO_2$) that caused hundreds to thousands of fatalities in Cameroon and Indonesia[22,23].

The methane emissions coincided with 21.6 ± 1.2 cm line-of-sight subsidence within Fentale between 15 and 23 January (Fig. 2N, S7). Modelling indicates a shallow source (<500 m depth) with a modest total volume loss (~10^5 m^3) (Text S2; Fig. S8). Gas, thermal, optical and deformation observations show a maximum in late January, followed by a rapid decline (Fig. 3). Starting from the end of January, low intensity thermal anomalies gradually extend towards the southeast, outlining an annular pattern centred on the deformation signal (Fig. S12). On 14 February, we observed a collapse of $5.6\times10^7 \pm 5.2\times10^6$ m^3 (~40 m vertical displacement) within the caldera, with a slightly larger footprint than the January deformation (Fig. 2O). This collapse coincided with a deep (~20 km) M_W 6.0 non-double-couple earthquake. Given its depth, the fault rupture likely did not directly cause the localised collapse, which may instead have been triggered by the associated ground shaking. Methane emission rates were relatively low (20.3 ± 12.0 t hr^{-1}) compared to the outburst in mid-January (Fig. 3A, Table S4).

During March, the thermal anomaly migrated gradually southeast, before stabilising along the inner edge of the caldera's southeastern margin (Fig. 2L, S12), where elevated temperatures persist throughout 2025. The low-lying plume remained present until 17 April (Fig. S14).

Methane emissions were less intense through March and April, with low emission rates (0.2–5.0 t d^{-1}) and detected enhancements confined to the low-lying areas of the caldera (Fig. 2C-D, Table S4). Steaming vents along the southern caldera wall were visible since mid-February and are spatially correlated with the ongoing thermal anomaly. Occasionally, plumes from these vents reach above the caldera wall, making them visible to the surrounding population (Fig. 2H-I, S14). Deformation rates decreased to -170 mm/yr from March 2025, although we still observed locally higher rates (~400 mm/yr) along the collapse margin (Fig. 2P, S10), potentially related to compaction. The ongoing activity suggests that the plumbing system is now partially open, but prevailing conditions in the area limit ground-based observations.

3 Where did the gases come from?

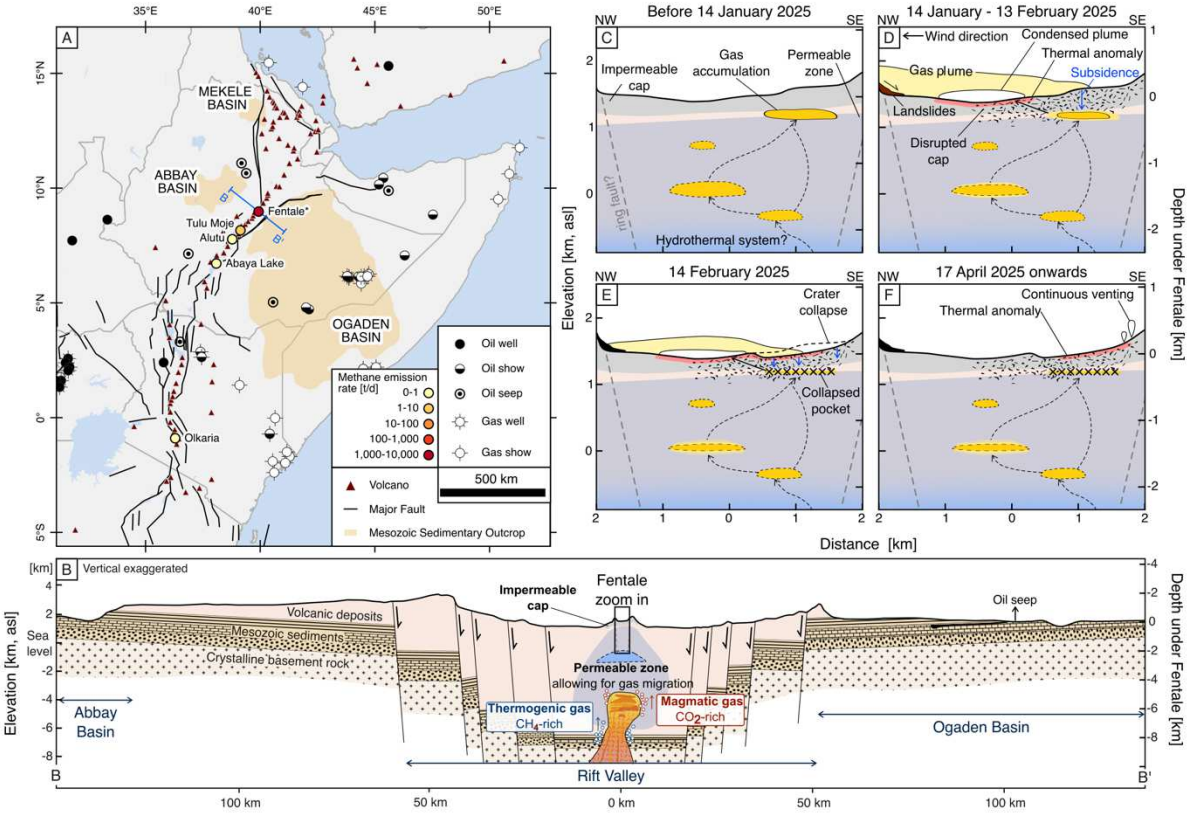

***Figure 4. Overview of the geology and volcanic system related to Fentale**. (A) Simplified regional map of the East African Rift (EAR) showing the spatial distribution of the Mesozoic sedimentary basins (orange areas)[24,25] within Ethiopia and the location of recent oil and gas exploration[25,26]. Ground-based measured methane emission rates are shown for volcanic systems along the EAR (Table S9). *Indicates outburst or transient event. (B) Schematic cross-section through the Main Ethiopian Rift (MER) (NW-SE trending profile shown in blue on A), showing simplified volcanic, sedimentary and basement units, highlighting the possible extent*

of the Mesozoic sediments across the rift. The volcanic system under Fentale is suggested as (1) CO_2 emissions from the shallow magmatic system (~5 km), (2) thermogenic CH_4 from sediment-magmatic interactions and (3) a permeable zone that allows for the migration of gas and accumulating in pockets, potentially hosting a hydrothermal system. (C-F) Conceptual models showing the proposed interpretation of the evolution at Fentale between January and April 2025, based on the observed activity by satellite remote sensing. Extent and depth covered is shown in (B).

Methane is typically only present in trace amounts in volcanic gases[27,28] and volcanoes are not considered to be a significant source of atmospheric methane[7]. Well-documented volcanoes in Europe emit <0.2 t d^{-1} each (Fig. 1C, S18)[5] and global volcanic methane emissions extrapolated from CO_2 emissions and CH_4/CO_2 ratios are <1 Tg yr^{-1}[29]. Higher methane emissions are known to occur in Sediment-Hosted Geothermal Systems (SHGS) where magmatic intrusions are emplaced within deep sedimentary basins (Fig. S17)[8]. For example, Lusi, Indonesia, has been emitting significant amounts of CO_2, methane, ethane and propane since 2006[11,30]. In SHGS, although CO_2 dominates (>50% vol), thermogenic methane is the second most abundant gas, with concentrations typically at percentage levels[8,11,31].

Fentale lies in the Main Ethiopian Rift (MER), which formed at 20-30 Myr within Mesozoic sedimentary basins[32]: the Abbay or Blue Nile Basin, the Ogaden Basin and the Mekele Basin[24,25]. These basins all contain significant hydrocarbon deposits within the same sequence of shales, limestones and sandstones at depths of 2-5 km and are targets for petroleum exploration[24,25]. Methane concentrations in gases sampled from the MER are several orders of magnitude higher than typical volcanic systems (Fig. S16) and can be up to 45 vol.% of the bulk gas[33]. Using previous ground-based surveys of CO_2 flux and CH_4/CO_2, we estimate methane emission rates at the MER volcanoes are 0.2-10.1 t d^{-1}, considerably higher than typical volcanic systems (<1 t d^{-1}, Fig. 1C, S16). Carbon isotope analysis ($\delta^{13}C$-CH_4 = of -31‰ to -18‰)[34] indicate that the methane is dominantly thermogenic. Within the rift, the high heat flow and consequent cracking of liquid hydrocarbons mean that the presence of oil is unlikely, but overmature dry gas, composed primarily of methane may be present[35]. We conclude that the Mesozoic sedimentary units are the source of the methane emitted during the 2025 Fentale outburst (Fig. 4A-B).

CO_2 emission rates during the Fentale outburst ($2.1x10^5 \pm 7.1\times10^4$ t d^{-1}) are near the upper end typical for volcanic eruptions ($13\text{-}2.6\times10^5$ t d^{-1}) and much higher than is typical for non-eruptive (passive) volcanic degassing ($1.0x10^{-2}\text{-}5.0\times10^4$ t d^{-1}) or background emissions from other EAR systems (250–500 t d^{-1})(Fig. 1D, S19, Table S9)[36]. The short duration (14 days) means the total mass emitted is equivalent to ~16% of the annual EAR emission from passive volcanic degassing ($5.0\times10^4 \pm 3.9\times10^4$ t d^{-1})[36,37]. Carbon isotope analysis (Abaya $\delta^{13}C$: −6.4‰ to −3.8‰) indicates that the CO_2 emissions are dominantly magmatic[33,38].

Although the CO_2 and methane at Fentale originate from two distinct sources (magmatic and sedimentary), the similarities in temporal and spatial emission patterns suggest they had accumulated in the same reservoir prior to the outburst. We conclude that the 2025 intrusion fractured a shallow impermeable seal, triggering an outburst of the accumulated gases (Fig. 4C-F). The exponential decline in methane emission following the outburst is consistent with the depressurization of the reservoir. The decline is punctuated by the collapse event on 14 February, which triggered a small resurgence in methane emissions. Simple mass balance calculations indicate that the localised subsidence and subsequent collapse (total volume ~8×10^7 m^3) could not have supplied the entire outburst (Text S4), and we conclude that this shallow reservoir represents the top of a larger, more complex system.

The outburst at Fentale indicates radically different behaviour compared to nearby volcanoes that show quasi-continuous degassing (Fig. 1C, Text S5, Fig. S16-18**)** where major rift-aligned faults provide open pathways for persistent emissions[37–39]. However, degassing patterns in the rift are spatially variable and with low fluxes seen in areas lacking permeable pathways[37]. Thus, we interpret the gas outburst at Fentale as fracturing of a previously sealed system. Taking long-term methane emission rates from quasi-continuously degassing MER volcanoes (0.5–1 t d^{-1}; Fig. 1C, Table S9) it would take 100-200 years to accumulate the 38 kt of methane released at Fentale in 2025. This coincides with the date of the last eruption in ~1810[40] and suggests that the system sealed soon after eruption and remained sealed until 2025, despite several smaller intrusions occurring[17,41–43].

4 Global Perspective

The 2025 Fentale outburst represents the first confirmed satellite observation of methane at a volcanic system and the first reported evidence that some volcanoes can emit significant

quantities of methane. This extends our understanding of the Earth's carbon degassing by demonstrating that sediment-magmatic interactions can produce significant methane emissions on very short timescales.

The methane emission rate at Fentale (33.8 ± 3.5 kt or 90% in 31 days; average rate of 1090 ± 113 t d^{-1}) is comparable in magnitude to major industrial blowouts, such as the 2015 Aliso Canyon event (average rate of 866 t d^{-1} over 112 days)[44], the 2019 Louisiana gas well blowout (average rate of 1289 t d^{-1} over 38 days)[45] and the 2023 Kazakhstan blowout (average rate of 639 t d^{-1} over 205 days)[46](Fig. 1C). The magnitude is the largest ever detected from a natural point source[11] but is <0.1% of the total annual emissions from the oil and gas industry[3]. Such sudden gas outbursts introduce significant invisible hazards. Both methane and CO_2 are colourless, odourless and can displace oxygen, impairing respiration and cognition, while high CO_2 levels (~10%) can cause unconsciousness and death[47]. The caldera shape constrained the emissions, limiting exposure but this demonstrates a neglected volcanic hazard.

The Fentale outburst resulted from magma interacting with overmature hydrocarbon-rich sediments. Similar interactions between magmatic intrusions and sedimentary material are thought to release carbon-based greenhouse gases, including thermogenic methane, during the formation of LIPs[10,16]. Simulations of the North Atlantic Igneous Province predict a peak emissions rate of 200-500 Mt yr^{-1} of carbon (90% thermogenic methane), sufficient to initiate climate change associated with the Paleocene–Eocene Thermal Maximum[2,48]. Our observations from Fentale provide the first modern analogue for processes proposed at LIPs, albeit at a much smaller scale. The short-lived, high-flux degassing contrasts sharply with the persistent low-level emissions from other EAR volcanoes, demonstrating the role of sealing and cap-rock integrity in regulating methane release. Although, the Fentale outburst is small compared to present-day anthropogenic emissions, its occurrence within a long-lived rift system shows that substantial methane emissions can still be produced on geological timescales.

The Fentale outburst reveals the potential for large, episodic emissions from rift-related volcanic systems. While it is the first such outburst to have been recorded, any outbursts prior to 2018, when TROPOMI became operational globally, would likely have gone undetected. Such natural outbursts are not fully accounted for in the natural atmospheric methane budget[4] or volcanic hazard assessment[49]. Continued satellite monitoring of volcanoes in rift and basin

environments is vital to quantify the frequency and global significance of these transient methane-release events and to constrain the links between magma-sediment interactions and the atmospheric methane budget.

5 Methods

Gas measurements

Quantification of methane plumes with TROPOMI

The Tropospheric Monitoring Instrument (TROPOMI), onboard the Sentinel-5P satellite, offers daily global observations of atmospheric column-averaged methane at down to 5.5 × 7 km² resolution at 13:30 local time over a ~2600 km swath, using measurements in the shortwave infrared (SWIR) near 2.3 μm and near-infrared (NIR) near 0.76 μm. For this analysis, we use version 02.05.00 of the operational TROPOMI Methane product[50], corrected for stripes[51] and filtered using: quality assurance (qa) value ≥ 0.4, SWIR aerosol optical thickness < 0.1, SWIR surface albedo > 0.05, SWIR cloud fraction < 0.015, and excluding observations over water. Methane emission plumes in the TROPOMI data are detected using a machine learning model described in Schuit et al. (2023)[52]. Detected plumes are provided to the Copernicus Atmospheric Monitoring Service (CAMS) and published on the Methane Hotspot Explorer webpage[53]. The detected plumes are quantified using the Integrated Mass Enhancement (IME) method to obtain an initial estimate of the emission rates[52]. The plume detection limit of TROPOMI is around 8 t hr^{-1}[52]; emissions below this could go undetected. We perform an additional, more detailed quantification using atmospheric transport modelling with an analytical inversion approach. For this analysis, we use TROPOMI data for days with clear methane plumes to generate the blended TROPOMI+GOSAT methane product using the machine learning model described in Balasus et al. (2023)[54], which corrects biases and artifacts in TROPOMI data by referencing methane measurements from the Greenhouse Gases Observing Satellite (GOSAT).

We use the Weather Research and Forecasting (WRF) model v4.1[55] to simulate methane concentration enhancements related to emissions from Fentale. We carry out the simulations at 9 × 9 km² resolution over a 900 × 900 km² domain and a nested 300 × 300 km² domain at a 3 × 3 km² resolution for January–March 2025. To best capture the plume, we perform several simulations using different transport schemes and either 6-hourly NCEP FNL (National Centers for Environmental Prediction Final)[20] or hourly ERA5 (European Centre for Medium-Range Weather Forecasts, ECMWF, Reanalysis v5)[19] reanalysis data as meteorological initial

and boundary condition inputs. CAMS global atmospheric forecasts[56] are used to provide initial and boundary chemical conditions.

We estimate daily methane emissions using a Bayesian inversion framework by minimizing the cost function[57] $\boldsymbol{J(x)}$ to optimize state vector $\mathbf{x}$ (Eq. 1). The state vector comprises daily emissions from Fentale, anthropogenic emissions of other background sectors (which include power industry, industrial combustion, buildings, transport, agriculture, fuel exploitation, industrial processes, and waste) taken from EDGAR (Emissions Database for Global Atmospheric Research) v2024[58], wetland emissions from WetCHARTs v1.3[59], and the daily domain mean and spatial deviation from the mean of the CAMS boundary conditions over the inversion domain. The cost function is defined as:

$$J(\mathbf{x}) = (\mathbf{x} - \mathbf{x_A})^{\mathrm{T}}\mathbf{S_A^{-1}}(\mathbf{x} - \mathbf{x_A}) + (\mathbf{y} - \mathbf{Kx})^{\mathrm{T}}\mathbf{S_O^{-1}}(\mathbf{y} - \mathbf{Kx}) \quad (1)$$

The optimized posterior fluxes are then determined as:

$$\hat{\mathbf{x}} = \mathbf{x_A} + \mathbf{S_A}\mathbf{K}^{\mathrm{T}}(\mathbf{K}\mathbf{S_A}\mathbf{K}^{\mathrm{T}} + \mathbf{S_o})^{-1}(\mathbf{y} - \mathbf{K}\mathbf{x_A}) \quad (2)$$

Here, $\hat{\mathbf{x}}$, is the posterior estimate, $\mathbf{x_A}$ is the prior state vector (set to 50 t/hr for the volcano), $\mathbf{S_A}$ is the prior error covariance (100% for the volcano emissions, 100% for background emissions, and 10% for boundary conditions), $\mathbf{S_o}$ is the diagonal observation error covariance estimated based on the standard deviation of the differences between the aggregated prior modelled concentrations and TROPOMI observations following Heald et al. (2004)[60], $\mathbf{K}$ is the Jacobian matrix relating emissions to concentrations, and $\mathbf{y}$ represents the TROPOMI observations. Modelled methane fields were convolved with TROPOMI's averaging kernels and resampled to match TROPOMI's pixel geometry and subsequently aggregated to 0.1° × 0.1° resolution for comparison with the observations to reduce the impact of small-scale spatial mismatches.

The diagonal elements of the inversion's averaging kernel matrix $\mathbf{A}$, indicate the sensitivity of the solution to the true state, with values ranging from 0 (posterior fully determined by the prior) to 1 (posterior fully determined by the observations). And is computed as:

$$\mathbf{A} = \mathbf{K^T}\mathbf{S_a}\mathbf{K}(\mathbf{K}\mathbf{S_a}\mathbf{K^T} + \mathbf{S_o})^{-1} \quad (3)$$

To identify simulations that best match the observed TROPOMI plume, we perform an ensemble of WRF simulations using NCEP FNL or ERA5 meteorological inputs, four planetary boundary layer (PBL) schemes (Table S1), and sampling times spanning ±3 hours around the TROPOMI overpass. Furthermore, we inject the emissions from the volcano at different elevations (0m (at surface level), 45m, 58m, 74m, 95m, 119m, 148m, and 182m) to capture any plume rise of the hot gas emitted. For each day, preliminary inversions were performed for all 448 model configurations, using identical background boundary conditions across all setups, optimizing both the spatial mean and variability of the CAMS boundary conditions and the volcano emissions. The model configuration yielding the inversion with the lowest posterior mismatch, quantified using the observation cost, was selected for the final emission estimation.

In the final inversions, we optimize both the spatial mean and variability of the CAMS-based background and the volcano emissions daily, while the emissions from other background sources are optimized over all days included for quantification. Days are included only if a distinct plume was observed in the TROPOMI data and if model-observation agreement was sufficient based on visual inspection. Emissions are quantified for seven days, including the six days with plumes detected using the machine learning approach. For all retained days, inversion averaging kernel values exceed 0.9 for the volcanic source, indicating high sensitivity of the posterior estimates to the TROPOMI observations.

To quantify uncertainty, we generate an ensemble of 18,144 inversions per orbit, varying key parameters and assumptions listed in Table S2. The 1-standard deviation ranges of this ensemble are reported as the uncertainties on the emission estimates. The emission rates quantified using the IME method and Bayesian inversion framework, along with their associated uncertainties, are presented in Table S3.

Quantification of methane and carbon dioxide plumes with GHGSat

GHGSat is a private company that designs and operates a constellation of 17 satellites (as of 20 December 2025) optimized for methane and carbon dioxide plume detection and quantification. The satellites travel in a sun-synchronous orbit, capturing solar backscatter radiation in the 1.6 μm spectral band with 25 - 30 m spatial resolution over targeted 15 × 12 – 15 × 30 km^2 retrieval domains[61]. The GHGSat measurement sequence takes approximately 20 seconds and, therefore, can be understood as a "snapshot" measurement of the methane column density within the retrieval domain.

GHGSat estimates the methane or carbon dioxide column density enhancement ΔΩ (units of moles per meter squared) above background in each of the approximately 275,000 ~25m × 25m grid cells in a retrieval domain. A methane or carbon dioxide emission is then characterized as a localized enhancement above the background value. In order to translate the column density enhancement measurement into an emission rate estimate Q, we use a cross-sectional flux method[57]:

$$Q = \frac{M_{out} u_{850hPa}}{L} \quad (4)$$

where $M_{out} = \Delta\Omega_{CH_4;out} \cdot A \cdot m_{CH_4}$ is the mass of the methane enhancement present outside of the caldera, integrated over downwind distance L, where we assume it is being transported with wind speed u_{850hPa} – the 850 hPa wind product from GEOS-FP[21], corresponding to an altitude of approximately 1500 m altitude – which is linearly interpolated to the observation time at the nearest spatial grid cell. The variable A is the area of the retrieval grid cells and $m_{CH_4} = 0.01604$ kg mol^{-1} is the molar mass of methane.

Quantification of methane and carbon dioxide plumes with Carbon Mapper

Carbon Mapper tasked and processed hyperspectral imagery from Planet's Tanager-1 satellite for CH_4 and CO_2 concentration enhancements. The Tanager satellite observes backscattered solar radiation between 400-2500 nm at 30 m spatial resolution and 5 nm spectral sampling[62]. Matched filter retrievals in the CH_4 (2200-2400 nm) and CO_2 (1960-2100 nm) absorption bands are applied to Tanager-1 images to derived concentration enhancement maps. Segmented plume images ("masks") for each acquisition are derived by selecting pixels above local background while also removing unconnected spurious concentration enhancements[62]. We then apply a form of the cross-sectional flux method to quantify CH_4 and CO_2 emissions. To do this, we identify the centre of mass of the segmented plume image (e.g., the region of highest concentration enhancement) and then define the plume axis as a line defined by two points of along the convex hull of the plume that result in maximum distance and pass through the centre of mass. For each cross section of the plume, the estimated emission rate (Q_i) is quantified as the following:

$$Q_i = U \int_a^b \Delta\Omega(x, y) dy \quad (5)$$

Where a, b represent a line perpendicular to the *i*th segment along the plume axis that lie on the plume mask. For wind fields, we used the ECMWF Integrated Forecast System (IFS) high-resolution model (9 km)[63]. The final estimated emission rate is the average of all *i* cross sections calculated along the plume axis, and the uncertainty is estimated as one standard deviation of all calculated emission rates.

Deformation

SAR data was acquired by the Italian Space Agency's (ASI) COSMO-SkyMed (CSK) and COSMO-SkyMed 2nd generation (CSG) satellites (Table S6), provided through the Committee on Earth Observation Satellites (CEOS) Global Volcano Early Warning and Eruption Response from Space (GVEWERS) programme and processed at the University of Bristol using GAMMA remote sensing software[64].

3D Displacements

To resolve three-dimensional ground displacement shown in Fig. 1A, we combined line-of-sight (LOS) range and azimuth displacement measurements from multiple SAR tracks. The study area was gridded at 250×250 m resolution in UTM coordinates. Within each grid cell, displacement measurements were averaged after excluding outliers beyond the 35th-65th percentile range to mitigate the effects of noise.

We inverted for the three-component displacement field (east-west, north-south, and vertical) using a weighted least-squares approach that incorporated look vectors for both ascending and descending Sentinel-1 (descending track 079 and ascending track 087) and COSMO-SkyMed tracks (descending track H4_04 and ascending track H4_02). The inversion included differential weighting to account for varying geometric sensitivity: east-west and vertical components were assigned higher confidence than the poorly constrained north-south component. Spatial smoothness regularization was implemented to ensure continuity across dataset boundaries and suppress noise, with directional weighting that applied stronger smoothing to the north-south component. Scalar offsets for each LOS dataset were simultaneously estimated within the inversion to account for reference frame differences. The final displacement field represents the cumulative deformation between December 2024 and late January 2025.

Deformation timeseries

Acquisition intervals vary between track but ranges from 1 to 31 days, with an average perpendicular baseline of 575 m (ranging from 2 to 1470 m). We apply a perpendicular baseline

threshold of 600 m to identify potential pairs for generating interferograms. The interferograms were generated for two temporal periods divided by the collapse event (14/02/2025; Table S6) using a high-resolution Pleiades DEM to correct for topography We process interferograms for an area at least 65 km^2 around Fentale Caldera at a resolution of 2 m (e.g., Fig. S6). We do not apply any corrections to mitigate the effect of atmospheric noise. We construct deformation timeseries using the LiCSBAS, a small-baseline time series analysis package[65]. To ensure a well-connected network, we use thresholds of average coherence (0.05) and coverage of unwrapped data (0.3) to identify low quality interferograms to remove. The choice of reference frame has a strong influence on the estimated timeseries. As we are interested in localised deformation within Fentale Caldera, we choose a reference area in the northeast portion of the caldera.

Signal anomaly detection

We applied the anomaly detection method approach developed by Giudicepietro et al., (2024)[66] to identify non-synchronous deformation patterns within our deformation timeseries. We first identify a representative timeseries of the widespread deformation signal in the area. For this we chose an area (10×10 pixels) in the centre of the broad subsidence signal beneath Fentale. For each pixel, we then calculate the correlation coefficient with the reference timeseries over a selected time interval that excludes any anomaly. To reduce computational intensity and ensure robustness, we retain timeseries with a correlation coefficient above 0.7. We then reconstruct the expected signal for each pixel based on correlation coefficient with the reference timeseries and calculate the residual between the reconstructed and original observed signal. We interpret deformation anomalies as regions that exhibit deformation patterns that diverge from the reference area trend.

Source modelling and estimating volume change

We model the CSK cumulative deformation images between December-February (Table S6) using a modified version of the geodetic inversion software Geodetic Bayesian Inversion Software (GBIS)[67,68]. The approach systematically downsamples the images using a nested-uniform approach between the near-field and far-field, which are manually delimited (Fig. S8), retaining approximately 1750 datapoints (~400 far-field, ~1400 near-field) in the ascending and descending data, respectively. Noise characteristics were approximated using a semi-variogram fitted to the far-field datapoints[68]. Given ambiguity in the source geometry, we invert for 8 analytical geometries of varying complexity (Table S7); point source[69], horizontal circular crack[70], spheroidal[71], rectangular dislocation sill[72], and planar and spheroidal compound dislocation models[73]. We use Bayesian Information Criterion (BIC)[74] to objectively assess the

preferred geometry. BIC compares misfits whilst applying a penalisation for model complexity (number of parameters) which is harsher than the related Akaike's Information Criterion (AIC)[75], suiting this case where the ratio of datapoints to model parameters is high. We report ΔBIC of each candidate model relative to a point source fit, using,

$$\Delta BIC = n\left(\ln \frac{(W)RSS_{point}}{(W)RSS_{candidate}}\right) + \left(k_{point} - k_{candidate}\right) \ln n \quad (6)$$

where n is the number of downsampled datapoints, *(W)RSS* is the (weighted) residual sum of squares, and k is the number of free parameters. The preferred geometry is the candidate model with the largest ΔBIC (Table S7). Based on the RMS and ΔBIC results, we determine that the rectangular dislocation sill and CGM-based planar sill with elongation were the geometries that best fit the data. We estimate the source volume at each timestep, this allows for direct comparison between ascending and descending datasets regardless of the viewing geometry or look-direction. We model each timestep using the optimal input parameters for an Okada sill (Table S8). By fixing all input variables except the opening, length and width, we can model variations in source volume for every timestep (Fig. S9).

Thermal Data

Thermal InfraRed (TIR) data were acquired by the Visible Infrared Imaging Radiometer Suite (VIIRS), on board the polar-orbiting Suomi National Polar-orbiting Partnership (Suomi NPP) and NOAA-20 satellites. The constellation enables the acquisition of approximately 4-6 images per day (daytime and nighttime) at a spatial resolution of 375 m.

VIIRS Level-1B calibrated radiance products were accessed through NASA's Land, Atmosphere Near-real-time Capability for EOS (LANCE: https://lance.modaps.eosdis.nasa.gov), and ingested into the MIROVA system[76,77] in near-real time (NRT).

Thermal anomaly detection was performed using the TIRVolcH algorithm[78], specifically designed to detect moderate-to-low-temperature volcanic hotspots. To prevent contamination from solar irradiance and reflectance while maintaining high sensitivity to subtle thermal variations, TIRVolcH operates only on nighttime scenes from VIIRS imaging band I5 centred at 11.45 μm.

When one or more anomalous pixels are detected, the associated TIR-based Volcanic Radiative Power (VRP_{TIR} – in watt) is quantified using the TIR-method[79]:

$$VRP_{TIR} = A_{Pix} \cdot k_{TIR} \cdot \sum_{i=1}^{N_{Pix}} (L_{TIR,hot_i} - L_{TIR,bg_i})$$

where A_{Pix} is the is the pixel area (140,625 m^2), k_{TIR} is the sensor-specific constant of proportionality[79], N_{Pix} is the number of hotspot-contaminated pixels, L_{TIR,hot_i} and L_{TIR,bg_i} ($W \cdot m^{-2} \cdot sr^{-1} \cdot \mu m^{-1}$) represent the integrated spectral radiance of the i-th hotspot-contaminated pixel and its corresponding background, respectively.

This approach is best suited for estimating radiative power under non-eruptive conditions and for volcanic systems dominated by surface temperatures ≲600 K. The approach holds an uncertainty of ±35%[79].

Optical analysis

Optical data was acquired by the European Sentinel-2 satellite and accessed through the Copernicus Browser (https://browser.dataspace.copernicus.eu/). High-resolution optical imagery was collected by the PlanetScope satellite of the Planet Lab constellation.

Optical cross-correlation

We use optical cross-correlation of two panchromatic Pléiades acquisitions (0.5 m) on 9 January and 24 April to measure the large horizontal displacement (several metres) associated with the collapse. The computation is done in the space domain with the free and open-source MicMac software[80] using a correlation window of 9×9 pixels and a step of 0.1 pixel. These Pléiades stereo acquisitions were also used independently to produce a pre- and a post-collapse DEM by photogrammetry using the MicMac software. We used the horizontal displacement estimated by cross-correlation to resample the post-collapse DEM before computing the DEM difference. Doing so, we make sure to compare the vertical positions of the same ground point before and after the collapse, and we therefore retrieve the 3D displacement of each ground point.

Near-Infrared (NIR) automated detection

We automatically extract the low-lying white plume within Fentale Caldera observed in the optical data. We use cloud free images in the Near-Infrared (NIR) band that have been cropped to the caldera. To extract the feature, we apply a threshold of 110 and 4000 to the NIR Band 8 Sentinel-2 and Planet images respectively to estimate the area of the low-lying white plume within the caldera. We examine the difference between the estimate areas for images captured within a few hours of each other (e.g., Sentinel-2 at 07:42 17-01-2025 and Planet at 08:04 17-

01-2025). We found good agreement between datasets (±0.02 km^2), which therefore did not require any further calibration.

6 Data availability

Sentinel-1 InSAR images and timeseries are provided open access through the COMET Volcanic and Magmatic Deformation Portal (https://comet.nerc.ac.uk/comet-volcano-portal/). COSMO-SkyMed (CSK) and COSMO-SkyMed 2nd generation (CSG) imagery was provided by the Agenzia Spaziale Italiana (ASI) via CEOS G-VEWERS programme.

The VIIRS data can be downloaded through NASA's Land, Atmosphere Near-real-time Capability for EOS (LANCE) data system (https://lance.modaps.eosdis.nasa.gov).

Pléiades images were provided under the CIEST2 (CNES-FormaTerre) initiative (image Pléiades ©CNES2025, distribution AIRBUS DS).

Carbon Mapper CH_4 and CO_2 plume visual datasets are available on the Carbon Mapper Data Portal (data.carbonmapper.org).

TROPOMI, Sentinel-2 and Sentinel-3 data are available at the Copernicus Data Hub (https://dataspace.copernicus.eu/). TROPOMI-based methane plume detections are available at https://apps.atmosphere.copernicus.eu/methane-explorer. The WRF-Chem model code can be downloaded at https://ruc.noaa.gov/wrf/wrf-chem/. The NCEP meteorology is available at https://gdex.ucar.edu/datasets/d083002. ERA5 Reanalysis data are available at https://cds.climate.copernicus.eu/datasets/reanalysis-era5-land?tab=download. GEOS-FP wind data can be downloaded at gmao.gsfc.nasa.gov/GMAO_products. The CAMS boundary conditions can be retrieved from https://ads.atmosphere.copernicus.eu/datasets/cams-global-atmospheric-composition-forecasts?tab=download. EDGARv2024 emissions are available at http://edgar.jrc.ec.europa.eu/dataset_ghg2024. GFEIv3 emissions can be retrieved from https://doi.org/10.7910/DVN/HH4EUM. WetCHARTs v1.3 emissions are available at https://daac.ornl.gov/cgi-bin/dsviewer.pl?ds_id=1915.

7 References

1. IPCC. *Climate Change 2021: The Physical Science Basis. Contribution of Working Group I to the Sixth Assessment Report of the Intergovernmental Panel on Climate Change*. vol. In Press (Cambridge University Press, Cambridge, United Kingdom and New York, NY, USA, 2021).

2. Jones, S. M., Hoggett, M., Greene, S. E. & Dunkley Jones, T. Large Igneous Province thermogenic greenhouse gas flux could have initiated Paleocene-Eocene Thermal Maximum climate change. *Nature Communications 2019 10:1* 10, 5547- (2019).

3. Saunois, M. *et al.* Global Methane Budget 2000-2020. *Earth Syst Sci Data* 17, 1873–1958 (2025).

4. Etiope, G., Ciotoli, G., Schwietzke, S. & Schoell, M. Gridded maps of geological methane emissions and their isotopic signature. *Earth Syst Sci Data* 11, (2019).

5. Etiope, G., Fridriksson, T., Italiano, F., Winiwarter, W. & Theloke, J. Natural emissions of methane from geothermal and volcanic sources in Europe. *Journal of Volcanology and Geothermal Research* 165, 76–86 (2007).

6. Etiope, G. & Schwietzke, S. Global geological methane emissions: An update of top-down and bottom-up estimates. *Elementa* 7, (2019).

7. Ryan, S. C., Dlugokencky, E. J., Tans, P. P. & Trudeau, M. E. Mauna Loa volcano is not a methane source: Implications for Mars. *Geophys Res Lett* 33, 12301 (2006).

8. Procesi, M., Ciotoli, G., Mazzini, A. & Etiope, G. Sediment-hosted geothermal systems: Review and first global mapping. *Earth Sci Rev* 192, 529–544 (2019).

9. Wignall, P. B. Large igneous provinces and mass extinctions. *Earth Sci Rev* 53, 1–33 (2001).

10. Aarnes, I., Svensen, H., Connolly, J. A. D. & Podladchikov, Y. Y. How contact metamorphism can trigger global climate changes: Modeling gas generation around igneous sills in sedimentary basins. *Geochim Cosmochim Acta* 74, 7179–7195 (2010).

11. Mazzini, A. *et al.* Relevant methane emission to the atmosphere from a geological gas manifestation. *Scientific Reports 2021 11:1* 11, 1–10 (2021).

12. Carn, S. A., Fioletov, V. E., Mclinden, C. A., Li, C. & Krotkov, N. A. A decade of global volcanic SO2 emissions measured from space. *Scientific Reports 2017 7:1* 7, 44095- (2017).

13. Pritchard, M. E. *et al.* Optimizing satellite resources for the global assessment and mitigation of volcanic hazards—Suggestions from the USGS Powell Center Volcano Remote Sensing Working Group. *Scientific Investigations Report* https://doi.org/10.3133/SIR20225116 (2022) doi:10.3133/SIR20225116.

14. Jacob, D. J. *et al.* Quantifying methane emissions from the global scale down to point sources using satellite observations of atmospheric methane. *Atmos Chem Phys* 22, 9617–9646 (2022).

15. Capriolo, M. *et al.* Massive methane fluxing from magma–sediment interaction in the end-Triassic Central Atlantic Magmatic Province. *Nature Communications 2021 12:1* 12, 5534- (2021).

16. Svensen, H. H., Jones, M. T. & Mather, T. A. Large Igneous Provinces and the Release of Thermogenic Volatiles from Sedimentary Basins. *Elements* 19, 282–288 (2023).

17. Way, L. *et al.* Real-time satellite monitoring of the 2024–2025 dyke intrusion sequence at Fentale-Dofen volcanoes, Ethiopia. *Bull Volcanol* 87, 100 (2025).

18. Lewi, E. *et al.* Scientific response to the 2024–2025 dyke intrusions in the Fentale-Dofen Region, Ethiopia: geophysical monitoring, surface manifestations, and hazard mapping. *Bull Volcanol* 87, 1–9 (2025).

19. Hersbach, H. *et al.* The ERA5 global reanalysis. *Quarterly Journal of the Royal Meteorological Society* 146, 1999–2049 (2020).

20. NCEP FNL, N. C. F. E. P. NCEP FNL Operational Model Global Tropospheric Analyses, continuing from July 1999. https://doi.org/10.5065/D6M043C6 (2000) doi:10.5065/D6M043C6.

21. Global Modeling and Assimilation Office Research. Global Modeling and Assimilation Office research: GEOS-FP version 5.21. *https://gmao.gsfc.nasa.gov/gmao-products/geos-fp/geos-fp-version-521-details_geos-fp/* https://gmao.gsfc.nasa.gov/gmao-products/geos-fp/geos-fp-version-521-details_geos-fp/ (2025).

22. Kusakabe, M., Ohsumi, T. & Aramaki, S. The Lake Nyos gas disaster: chemical and isotopic evidence in waters and dissolved gases from three Cameroonian crater lakes, Nyos, Monoun and Wum. *Journal of Volcanology and Geothermal Research* 39, 167–185 (1989).

23. Allard, P., Dajlevic, D. & Delarue, C. Origin of carbon dioxide emanation from the 1979 Dieng eruption, Indonesia: Implications for the origin of the 1986 Nyos catastrophe. *Journal of Volcanology and Geothermal Research* 39, 195–206 (1989).

24. Hunegnaw, A., Sage, L. & Gonnard, R. HYDROCARBON POTENTIAL OF THE INTRACRATONIC OGADEN BASIN, SE ETHIOPIA. *Journal of Petroleum Geology* 21, 401–425 (1998).

25. Wolela, A. SOURCE ROCK POTENTIAL OF THE BLUE NILE (ABAY) BASIN, ETHIOPIA. *Journal of Petroleum Geology* 30, 389–402 (2007).

26. Persits, F. M. *et al.* Maps showing geology, oil and gas fields and geological provinces of Africa. *Open-File Report* https://doi.org/10.3133/OFR97470A (1997) doi:10.3133/OFR97470A.

27. Capaccioni, B. *et al.* Light hydrocarbons in gas-emissions from volcanic areas and geothermal fields. *Geochem J* 27, 7–17 (1993).

28. Taran, Y. A. & Giggenbach, W. F. Geochemistry of Light Hydrocarbons in Subduction-Related Volcanic and Hydrothermal Fluids. *Volcanic, Geothermal, and Ore-Forming Fluids* 61–74 (2005) doi:10.5382/SP.10.04.

29. Etiope, G., Lassey, K. R., Klusman, R. W. & Boschi, E. Reappraisal of the fossil methane budget and related emission from geologic sources. *Geophys Res Lett* 35, (2008).

30. Mazzini, A. *et al.* Extensive oil, ethane and propane discharge at the mega seepage system of Lusi, Indonesia. *Communications Earth & Environment 2025 6:1* 6, 854- (2025).

31. Ciotoli, G. *et al.* Tiber delta CO2-CH4 degassing: A possible hybrid, tectonically active Sediment-Hosted Geothermal System near Rome. *J Geophys Res Solid Earth* 121, 48–69 (2016).

32. Chernet, T., Hart, W. K., Aronson, J. L. & Walter, R. C. New age constraints on the timing of volcanism and tectonism in the northern Main Ethiopian Rift–southern Afar transition zone (Ethiopia). *Journal of Volcanology and Geothermal Research* 80, 267–280 (1998).

33. Minissale, A. *et al.* Geothermal potential and origin of natural thermal fluids in the northern Lake Abaya area, Main Ethiopian Rift, East Africa. *Journal of Volcanology and Geothermal Research* 336, 1–18 (2017).

34. Darling, W. G. Hydrothermal hydrocarbon gases: 2, Application in the East African Rift System. *Applied Geochemistry* 13, 825–840 (1998).

35. Kutovaya, A., Kroeger, K. F., Seebeck, H., Back, S. & Littke, R. Thermal Effects of Magmatism on Surrounding Sediments and Petroleum Systems in the Northern Offshore Taranaki Basin, New Zealand. *Geosciences 2019, Vol. 9, Page 288* 9, 288 (2019).

36. Werner, C. *et al.* Carbon Dioxide Emissions from Subaerial Volcanic Regions: Two Decades in Review. in *Deep Carbon. Past to Present* 188–236 (Cambridge University Press, 2019).

37. Hunt, J. A., Zafu, A., Mather, T. A., Pyle, D. M. & Barry, P. H. Spatially Variable CO2 Degassing in the Main Ethiopian Rift: Implications for Magma Storage, Volatile Transport, and Rift-Related Emissions. *Geochemistry, Geophysics, Geosystems* 18, 3714–3737 (2017).

38. Hutchison, W. *et al.* Gas Emissions and Subsurface Architecture of Fault-Controlled Geothermal Systems: A Case Study of the North Abaya Geothermal Area. *Geochemistry, Geophysics, Geosystems* 24, e2022GC010822 (2023).

39. Hutchison, W., Mather, T. A., Pyle, D. M., Biggs, J. & Yirgu, G. Structural controls on fluid pathways in an active rift system: A case study of the Aluto volcanic complex. https://doi.org/10.1130/GES01119.1 (2015) doi:10.1130/GES01119.1.

40. Williams, F. M., Williams, M. A. J. & Aumento, F. Tensional fissures and crustal extension rates in the northern part of the Main Ethiopian Rift. *Journal of African Earth Sciences* 38, 183–197 (2004).

41. Temtime, T., Biggs, J., Lewi, E. & Ayele, A. Evidence for Active Rhyolitic dike Intrusion in the Northern Main Ethiopian Rift from the 2015 Fentale Seismic Swarm. *Geochemistry, Geophysics, Geosystems* 21, (2020).

42. Ayele, A., Luckett, R., Baptie, B. & Whaler, K. The 2015 earthquake swarm in the Fentale volcanic complex (FVC): A geohazard risk for Ethiopia's commercial route to the Djibouti port. *Journal of African Earth Sciences* 213, 105236 (2024).

43. Keir, D. *et al.* The 2024 Fentale Diking Episode in a Slow Extending Continental Rift. *Geophys Res Lett* 52, (2025).

44. Conley, S. *et al.* Methane emissions from the 2015 Aliso Canyon blowout in Los Angeles, CA. *Science (1979)* 351, 1317–1320 (2016).

45. Maasakkers, J. D. *et al.* Reconstructing and quantifying methane emissions from the full duration of a 38-day natural gas well blowout using space-based observations. *Remote Sens Environ* 270, 112755 (2022).

46. Guanter, L. *et al.* Multisatellite Data Depicts a Record-Breaking Methane Leak from a Well Blowout. *Environ Sci Technol Lett* 11, 825–830 (2024).

47. Balagizi, C. M. *et al.* Natural hazards in Goma and the surrounding villages, East African Rift System. *Natural Hazards* 93, 31–66 (2018).

48. Svensen, H. *et al.* Release of methane from a volcanic basin as a mechanism for initial Eocene global warming. *Nature 2004 429:6991* 429, 542–545 (2004).

49. Biggs, J. *et al.* Volcanic activity and hazard in the East African Rift Zone. *Nature Communications 2021 12:1* 12, 6881- (2021).

Methods References

50. Lorente, A., Borsdorff, T., Martinez-Velarte, M. C. & Landgraf, J. Accounting for surface reflectance spectral features in TROPOMI methane retrievals. *Atmos Meas Tech* 16, 1597–1608 (2023).

51. Borsdorff, T. *et al.* Mapping carbon monoxide pollution from space down to city scales with daily global coverage. *Atmos Meas Tech* 11, 5507–5518 (2018).

52. Schuit, B. J. *et al.* Automated detection and monitoring of methane super-emitters using satellite data. *Atmos Chem Phys* 23, 9071–9098 (2023).

53. CAMS. CAMS Methane Hotspot Explorer. https://atmosphere.copernicus.eu/ghg-services/cams-methane-hotspot-explorer (2025).

54. Balasus, N. *et al.* A blended TROPOMI+GOSAT satellite data product for atmospheric methane using machine learning to correct retrieval biases. *Atmos Meas Tech* 16, 3787–3807 (2023).

55. Powers, J. G. *et al.* The Weather Research and Forecasting Model: Overview, System Efforts, and Future Directions. *Bull Am Meteorol Soc* 98, 1717–1737 (2017).

56. CAMS. CAMS global atmospheric composition forecasts. *ECMWF* https://doi.org/https://doi.org/10.24381/04A0B097 (2021) doi:https://doi.org/10.24381/04A0B097.

57. Jacob, D. J. *et al.* Satellite observations of atmospheric methane and their value for quantifying methane emissions. *Atmos Chem Phys* 16, 14371–14396 (2016).

58. Crippa, Monica. *et al. GHG Emissions of All World Countries 2024*. (2024) doi:doi:10.2760/4002897.

59. Bloom, A. A. *et al.* A global wetland methane emissions and uncertainty dataset for atmospheric chemical transport models (WetCHARTs version 1.3.1). *Geosci Model Dev* 10, 2141–2156 (2017).

60. Heald, C. L. *et al.* Comparative inverse analysis of satellite (MOPITT) and aircraft (TRACE-P) observations to estimate Asian sources of carbon monoxide. *Journal of Geophysical Research: Atmospheres* 109, 1–17 (2004).

61. Jervis, D. *et al.* The GHGSat-D imaging spectrometer. *Atmos Meas Tech* 14, 2127–2140 (2021).

62. Duren, R. *et al.* The Carbon Mapper emissions monitoring system. *Atmos Meas Tech* 18, 6933–6958 (2025).

63. Open-Meteo. ECMWF Weather Forecast API. *https://open-meteo.com* https://open-meteo.com (2025).

64. Werner, C., Wegmüller, U., Strozzi, T. & Wiesmann, A. GAMMA SAR AND INTERFEROMETRIC PROCESSING SOFTWARE. http://www.gamma-rs.ch (2000).

65. Morishita, Y. *et al.* LiCSBAS: An Open-Source InSAR Time Series Analysis Package Integrated with the LiCSAR Automated Sentinel-1 InSAR Processor. *Remote Sensing 2020, Vol. 12, Page 424* 12, 424 (2020).

66. Giudicepietro, F. *et al.* First evidence of a geodetic anomaly in the Campi Flegrei caldera (Italy) ground deformation pattern revealed by DInSAR and GNSS measurements during the 2021–2023 escalating unrest phase. *International Journal of Applied Earth Observation and Geoinformation* 132, 104060 (2024).

67. Ireland, B., Biggs, J., Anantrasirichai, N., Albino, F. & Dualeh, E. W. Towards Systematic Modelling of Volcano Deformation Sources using Automatically-Generated InSAR Products. *Authorea Preprints* https://doi.org/10.22541/ESSOAR.175767337.70239282/V1 (2025) doi:10.22541/ESSOAR.175767337.70239282/V1.

68. Bagnardi, M. & Hooper, A. Inversion of Surface Deformation Data for Rapid Estimates of Source Parameters and Uncertainties: A Bayesian Approach. *Geochemistry, Geophysics, Geosystems* 19, 2194–2211 (2018).

69. Mogi, K. Relations between the eruptions of various volcanoes and the deformations of the ground surfaces around them. *Bulletin of the Earthquake Research Institute* 36, 99–134 (1958).

70. Sun, R. J. Theoretical size of hydraulically induced horizontal fractures and corresponding surface uplift in an idealized medium. *J Geophys Res* 74, 5995–6011 (1969).

71. Cervelli, P. F., Cervelli & F., P. Analytical Expressions for Deformation from an Arbitrarily Oriented Spheroid in a Half-Space. *AGUFM* 2013, V44C-06 (2013).

72. Okada, Y. SURFACE DEFORMATION DUE TO SHEAR AND TENSILE FAULTS IN A HALF-SPACE. *Bulletin of the Seismological Society of America* 75, 1135–1154 (1985).

73. Nikkhoo, M., Walter, T. R., Lundgren, P. R. & Prats-Iraola, P. Compound dislocation models (CDMs) for volcano deformation analyses. *Geophys J Int* 208, 877–894 (2017).

74. Schwarz, G. Estimating the Dimension of a Model. *https://doi.org/10.1214/aos/1176344136* 6, 461–464 (1978).

75. Akaike, H. A New Look at the Statistical Model Identification. *IEEE Trans Automat Contr* 19, 716–723 (1974).

76. Coppola, D., Laiolo, M., Cigolini, C., Delle Donne, D. & Ripepe, M. Enhanced volcanic hot-spot detection using MODIS IR data: results from the MIROVA system. *Geol Soc Spec Publ* 426, 181–205 (2016).

77. Campus, A., Laiolo, M., Massimetti, F. & Coppola, D. The Transition from MODIS to VIIRS for Global Volcano Thermal Monitoring. *Sensors* 22, 1713 (2022).

78. Aveni, S., Laiolo, M., Campus, A., Massimetti, F. & Coppola, D. TIRVolcH: Thermal Infrared Recognition of Volcanic Hotspots. A single band TIR-based algorithm to detect low-to-high thermal anomalies in volcanic regions. *Remote Sens Environ* 315, 114388 (2024).

79. Aveni, S., Pailot-Bonnétat, S., Rouwet, D., Harris, A. J. L. & Coppola, D. Volcanic Radiative Power Retrieval From Moderate-to-Low-Temperature Features Using a Single TIR Band: Validation Using Volcanic Crater Lakes and Hydrothermal Systems. *Geophys Res Lett* 52, e2024GL113324 (2025).

80. Rupnik, E., Daakir, M. & Pierrot Deseilligny, M. MicMac – a free, open-source solution for photogrammetry. *Open Geospatial Data, Software and Standards 2017 2:1* 2, 1–9 (2017).

8 Acknowledgements

E.W.D was supported by a European Space Agency (ESA) Living Planet Fellowship (VolcScatter). **E.W.D., J.B., L.W., W.Z., B.I.,** and **T.D.,** were supported by the NERC Centre for the Observation and Modelling of Earthquakes, Volcanoes, and Tectonics (COMET, http://comet.nerc.ac.uk) a partnership between UK Universities and the British Geological Survey. **J.B., L.W., W.Z., B.I., T.D.,** and **E.L** also received funding from the European Research Council (ERC) under the European Union's Horizon 2020 research and innovation programme (MAST; Grant No. 101003173). **L.W.** was supported by a University of Bristol Postgraduate Scholarship. **J.S.** was supported by ongoing Discovery Grant support from the Natural Sciences and Engineering Research Council of Canada (NSERC). **W.H.** is funded by a UKRI Future Leaders Fellowship (MR/S033505/1). **G.E.** was supported by the ENGAGE project, funded by European Union through the Romanian's National Recovery and Resilience Plan (contract n. 760039/23.05.2023). **S.S.** acknowledges funding from the IMEO Science Studies Programme contract DTIE22-EN5036. **M.D.** acknowledges funding from the ESA MEDUSA project. **J.D.M.** acknowledges funding from the Copernicus Atmosphere Monitoring Service CAMS2_53a. **S.A.** was supported by the 'Piano Nazionale di Ripresa e Resilienza' (PNRR). **M.N** is supported by funding from the National Science Foundation (NSF EAR-1936254)

The authors acknowledge the support of SURF Cooperative, as part of this work was carried out on the Dutch national e-infrastructure. We thank the team that realized the TROPOMI instrument and its data products, consisting of the partnership between Airbus Defence and Space Netherlands, KNMI, SRON, and TNO and commissioned by NSO and ESA. The Sentinel-5 Precursor and Sentinel-2 are part of the EU Copernicus program, and Copernicus (modified) Sentinel-5P data (2025) and Sentinel-2 data (2025) have been used. Generated using/Contains modified Copernicus Atmosphere Monitoring Service information 2025. Neither the European Commission nor ECMWF is responsible for any use that may be made of the Copernicus information or data it contains.

We acknowledge support from the Addis Ababa University, Ethiopian Geological Institute and Ethiopian Disaster Risk Management Commission. We would also like to acknowledge Zak Thompson for aiding in the compiling literature on volcanic carbon dioxide and methane emission rates and Jake Lowenstern for providing useful discussion and input during and following the unrest event.

9 Author Contributions

E.W.D - Methodology, Data curation, Investigation, Formal analysis, Visualization, Project administration, Writing – original draft, Writing – review & editing; **J.B.** - Conceptualization, Methodology, Project administration, Supervision, Writing – original draft, Writing – review & editing; **S.S.** - Methodology, Data curation, Investigation, Formal analysis, Visualization, Writing – original draft, Writing – review & editing; **J.S.** - Conceptualization, Supervision, Writing – review & editing; **W.H**. - Investigation, Formal analysis, Visualization, Writing – original draft, Writing – review & editing; **G.E.** - Conceptualization, Investigation, Writing – original draft, Writing – review & editing; **D.J.** - Data curation, Investigation, Visualization, Writing – original draft, Writing – review & editing; **L.W**. - Investigation, Formal analysis, Writing – review & editing; **M.D.** - Investigation, Writing – review & editing; **J.D.M.** - Supervision, Writing – original draft, Writing – review & editing; **S.A.** - Methodology, Investigation, Formal analysis, Visualization, Writing – review & editing; **D.Cu.** - Visualization, Supervision, Writing – original draft; **B.I.** - Formal analysis, Visualization, Writing – original draft; **R.G.** - Data curation, Supervision, Writing – review & editing; **M.G.** - Data curation, Investigation; **A.R.** - Data curation; **W.Z.** - Data curation, Software; **T.D.** - Visualization, Writing – original draft; **K.H.** - Methodology, Software; **D.Co.** - Supervision,

Writing – review & editing; **A.H.** - Formal analysis; **R.P.** - Writing – review & editing; **M.N.** - Investigation, Writing – original draft; **E.L.** - Conceptualization, Writing – review & editing

10 Ethics declaration

The authors declare no competing interests.

Additional information Supplementary Information is available for this paper**.**

Correspondence Correspondence and requests for materials should be addressed to Edna W. Dualeh (edna.dualeh@bristol.ac.uk)

Supplementary Files

This is a list of supplementary files associated with this preprint. Click to download.

- FentaleSupplementary.pdf